

# **EMA 521 Final Project**

Author: Bryce Quinton

December 14<sup>th</sup>, 2025

Engineering Mechanics and Aerospace  
Department of Mechanical Engineering  
University of Wisconsin – Madison

# 1. 2D Analysis

## 1.1. Thin Airfoil Theory

Thin Airfoil Theory states that,

$$c_l = 2\pi(\alpha + \alpha_{L'=0}) \quad (4.60)$$

where  $c_l$  is the lift coefficient,  $\alpha$  is the angle of attack, and  $\alpha_{L'=0}$  is the angle of attack at which the airfoil has zero lift. From Anderson equation 4.61 defines,

$$\alpha_{L'=0} = \frac{1}{\pi} \int_0^\pi \frac{dz}{dx} (\cos \theta_0 - 1) d\theta_0 \quad (4.61)$$

By definition the slope of a NACA 4-digit airfoil is,

$$\begin{aligned} \frac{dz_c}{dx} &= \frac{2m}{p^2}(p-x) \quad \text{for } 0 \leq x \leq p \\ \frac{dz_c}{dx} &= \frac{2m}{(1-p)^2}(p-x) \quad \text{for } p < x \leq 1 \end{aligned}$$

where  $m$  is the max camber percentage and  $p$  is the location of max camber, both as percentages of the cord length. With the use of,

$$x = \frac{1 - \cos \theta_0}{2}$$

the slope of the camber line to be written as a function of  $\theta_0$ . This result allows the integral in equation 4.61 to be evaluated. This results in,

$$\alpha_{L'=0} = \frac{m}{4\pi p^2(p-1)^2} [(8p-6)(\pi p^2 - 2p\theta_p + \theta_p) + 8(2p^2 - 3p + 1) \sin \theta_p + (2p-1) \sin 2\theta_p]$$

where,

$$\theta_p = \arccos(1 - 2p)$$

Plotting equation 4.60 as a function of angle of attack can be seen in Figure 1.1.1.

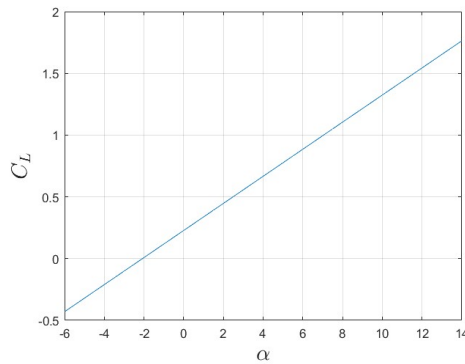


Figure 1.1.1. Lift coefficient vs angle of attack of NACA 2412 using Thin Airfoil Theory.

## 1.2. Vortex Panel Method

The pressure coefficient of the NACA 2412 airfoil can be predicted by use of the Vortex Panel Method, which is a numerical solution by splitting up the airfoil into finite, straight panels. A linear circulation distribution will be used along the wall of the airfoil, so a vortice will be placed at the midpoint of each panel to approximate the circulation created due to the flow around the airfoil.

$$V_n = - \sum_{j=1}^n \frac{\gamma}{2\pi} \int_j \frac{\partial \theta_{i,j}}{\partial n_i} ds_j \quad (4.77)$$

Equation 4.77 provides n-equations. Additionally, a boundary condition will be enforced at the wall of each panel to ensure no penetration of the fluid. Therefore,

$$V_{\infty,n} + V_n = 0 \quad (4.78)$$

This results in an infinite number of solutions; however, the Kutta Condition must also be satisfied. Which states there must be no circulation at the trailing edge. Therefore,

$$\gamma_i = -\gamma_{i-1} \quad (4.81)$$

By solving numerically solving the velocities at the wall of each panel, the pressure coefficient on each panel can be solved,

$$C_p = 1 - \left( \frac{V_n}{V_{\infty}} \right)^2 \quad (3.38)$$

By use of the geometry of each panel the lift and drag coefficients for the entire airfoil can be resulted. Overlaying the lift coefficient results of the vortex panel method onto that of thin airfoil theory can be seen in Figure 1.2.1.

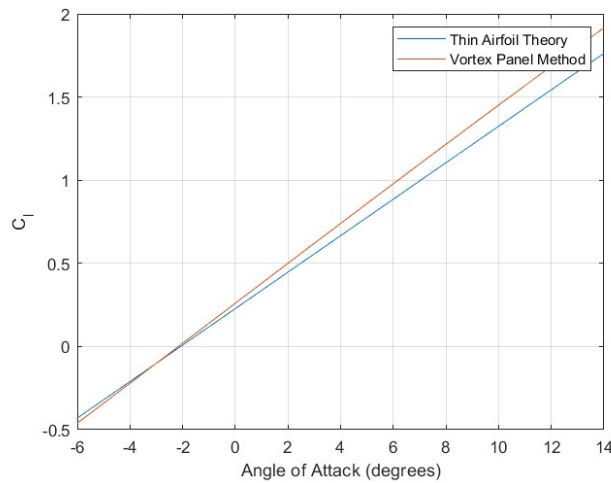


Figure 1.2.1. Lift coefficient vs angle of attack of NACA 2412 using Thin Airfoil Theory and Vortex Panel Method.

Drag coefficients also resulted from this method which can be seen in Figure 1.2.2 across low angles of attack.

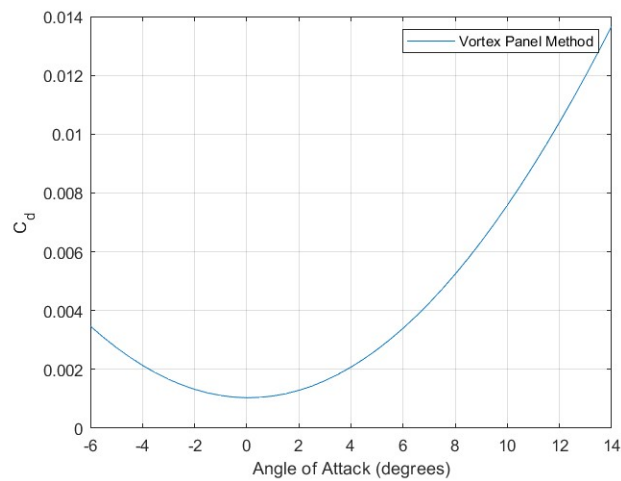


Figure 1.2.2. Drag coefficient vs angle of attack of NACA 2412 using Vortex Panel Method.

### 1.3. XFLR5

The final method that will be used in the analysis of the NACA2412 airfoil will be via the software XFLR5. XFLR5 provided the geometry of the NACA2412 airfoil divided into 200 panels. For the parameters of the analysis, a Reynold's Number of 100,000 was used as this is a reasonable value for a low-speed flow under standard atmospheric conditions. The output of the lift and drag coefficients over a range of low angles of attack are provided in Figure 1.3.1 and Figure 1.3.2, respectively.

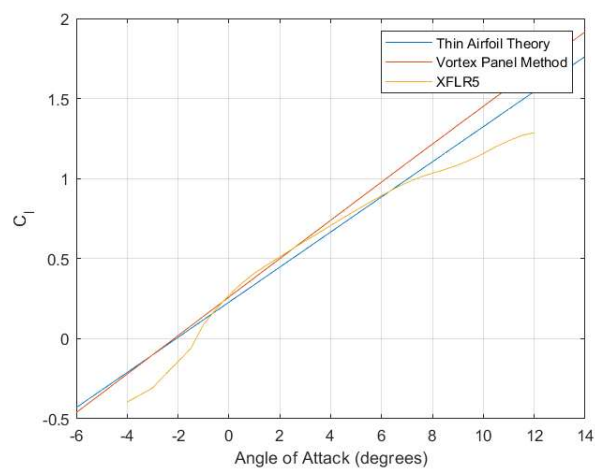


Figure 1.3.1. Lift coefficient vs angle of attack of NACA 2412 using Thin Airfoil Theory, Vortex Panel Method, and XFLR5.

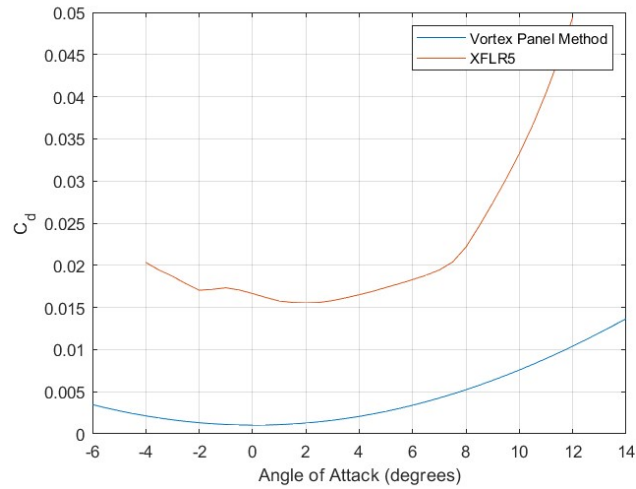


Figure 1.3.2. Drag coefficient vs angle of attack of NACA 2412 using Vortex Panel Method and XFLR5.

## 1.4. Model Comparison

By inspection of Figure 1.3.1, along with the analysis methods associated with it, it can be seen that both Thin Airfoil Theory and Vortex Panel Method closely model the lift coefficient for angles of attack in the range  $-1^\circ$  to  $7^\circ$ , which aligns with the assumption of both methods that the angle of attack is small. The limitation of thin Airfoil Theory is that it does not account for the thickness of the airfoil, therefore, more inaccuracies will result from Thin Airfoil Theory compared to Vortex Panel Method. This can be seen by the lift coefficient of the Vortex Panel Method resembling the XFLR5 better during low angles of attack. Both Vortex Panel Method and Thin Airfoil Theory do not simulate flow separation, so stalling will not be accounted for in the results, which is why both methods become inaccurate beyond  $8^\circ$ .

For the drag coefficients seen in Figure 1.3.2, the Vortex Panel Method closely resembles the shape of the XFLR5 data during low angles of attack, however not the magnitude. This discrepancy is because Vortex Panel Method does not account for skin friction and XFLR5 does. This is a significant error because skin friction is the leading cause of drag for a slender body. This aligns with the plot as Vortex Panel Method shows much lower drag coefficients compared to the XFLR5 output.

## 1.5. Mach Number Effect

In subsonic flow, as the Mach number increases the flow over an airfoil will be affected and thus changing the result of a lift coefficients. A correction factor to the Vortex Panel Method described in section 1.2 will be applied. This correction factor is defined by Prandtl-Glauert Compressibility Correction,

$$C_l = \frac{C_{l,0}}{\sqrt{1 - Ma^2}} \quad (11.52)$$

The correction factor will be applied to the Vortex Panel Method for the NACA2412 airfoil across 3 subsonic Ma numbers (0.1, 0.4, and 0.7). The effects of these corrections can be seen in Figure 1.5.1.

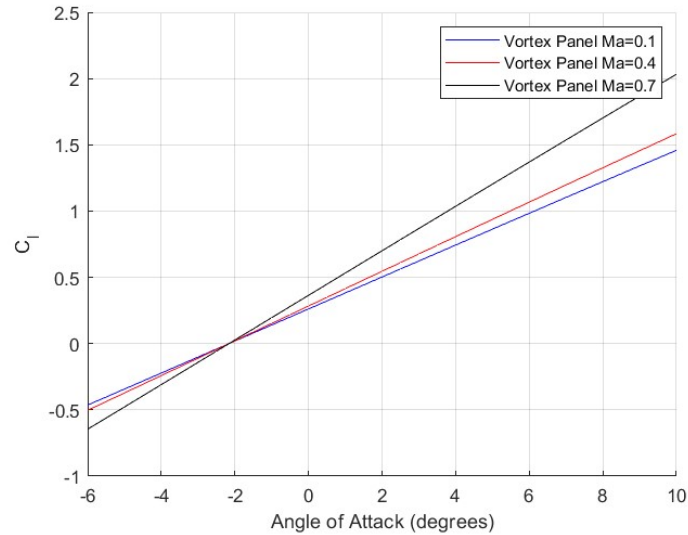


Figure 1.5.1. Prandtl-Glauert Compressibility Correction for NACA2412 across various Mach numbers with Vortex Panel Method.

The results show that with an increase in Mach number,  $\frac{dc_l}{d\alpha}$  increases. Now to compare the accuracy of correction factors at each Mach number, XFLR5 can be used to apply compressibility corrections to the previous XFLR5 results. Note that the Vortex Panel Method is using the Prandtl-Glauert Compressibility correction while XFLR5 uses the Karman-Tsien correction. In Figure 1.5.2, Figure 1.5.3, and Figure 1.5.4, each Vortex Panel Method correction is overlaid with the output of XFLR5 at the same Mach number.

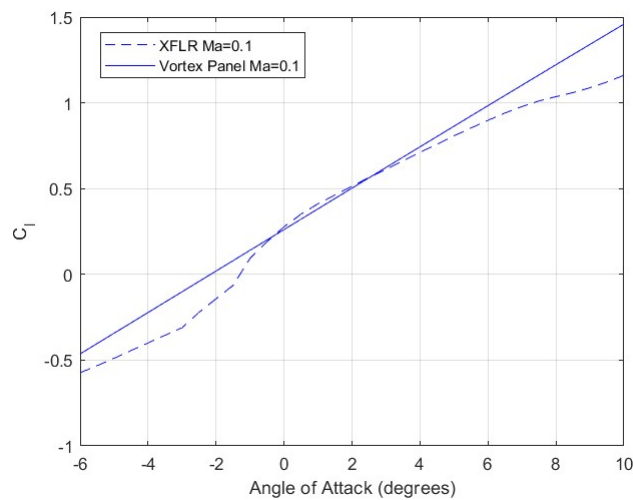


Figure 1.5.2. Lift Coefficient vs Angle of Attack of Vortex Panel Method and XFLR5 at Ma = 0.1

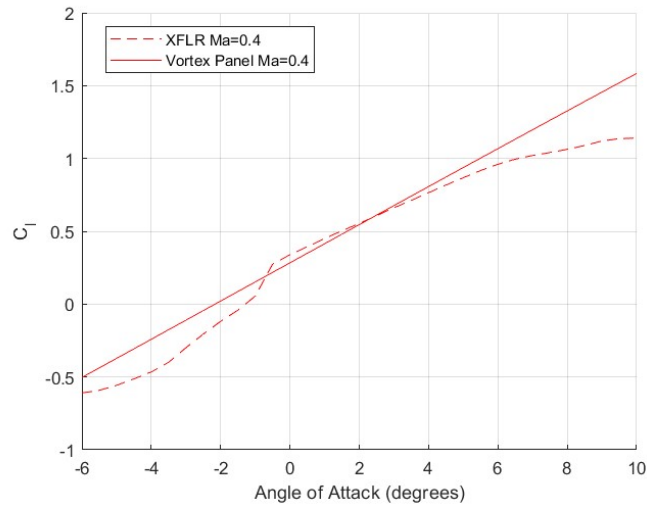


Figure 1.5.3. Lift Coefficient vs Angle of Attack of Vortex Panel Method and XFLR5 at  $Ma = 0.4$

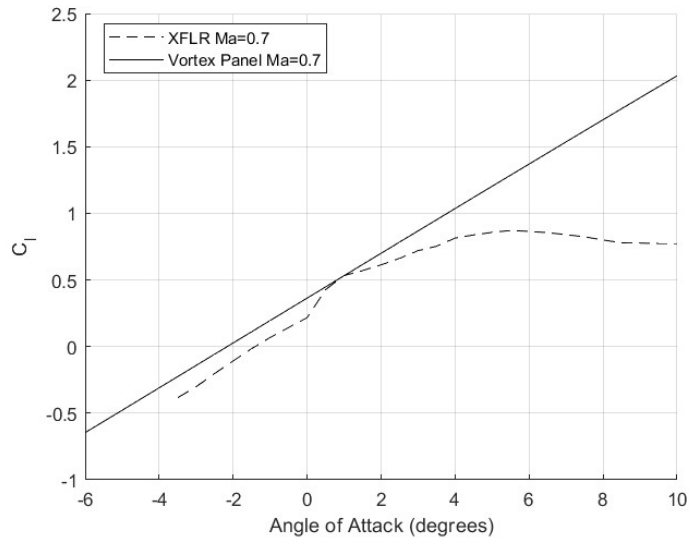


Figure 1.5.4. Lift Coefficient vs Angle of Attack of Vortex Panel Method and XFLR5 at  $Ma = 0.7$

At each individual Mach number, it can be observed that  $\frac{dC_l}{d\alpha}$  is closely related between the Vortex Panel Method and the XFLR5 output, at low angles of attack. This range of accurate angles of attacks differs as Mach number increases. From the XFLR5 output data shown in Figure 1.5.5, the angle at which stall begins to occur is lower with increasing Mach number which limits the validity of the Vortex Panel Method at high, sub-sonic Mach numbers.

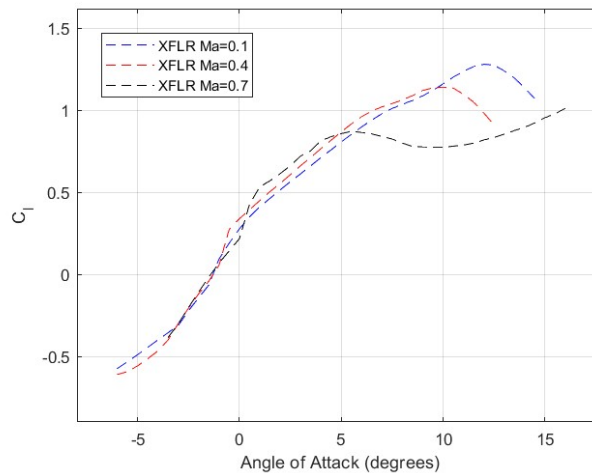


Figure 1.5.5. Compressibility Correction for NACA2412 across various Mach numbers with XFLR5.

## 1.6. NACA Airfoil Variations: Max Camber Location

The second digit of a 4-digit NACA airfoil designates the location at which the max camber exists. This number is given as a percentage of the length of the cord. This section will look at the effects on lift coefficients of changing this location because prior to this all analysis of NACA airfoils has held this parameter as a constant so it is important to note its effects. The Mach number will act as an additional independent variable for this section of the analysis. The three airfoils that will be analyzed are NACA 2212, NACA 2512, and NACA 2812. This places the max camber location at  $0.2c$ ,  $0.5c$ , and  $0.8c$ , respectively, from the leading edge, where  $c$  is the cord length.

Each airfoil will be compared by both Vortex Panel Method and XFLR5. This process will be evaluated at Mach numbers 0.1, 0.4, and 0.7. The results are shown in Figure 1.6.1, Figure 1.6.2, and Figure 1.6.3.

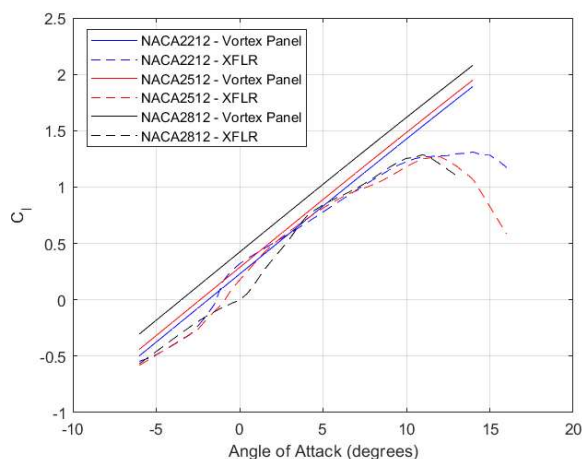


Figure 1.6.1. Comparison of airfoils with varying max camber location using Vortex Panel Method and XFLR5 at  $Ma = 0.1$



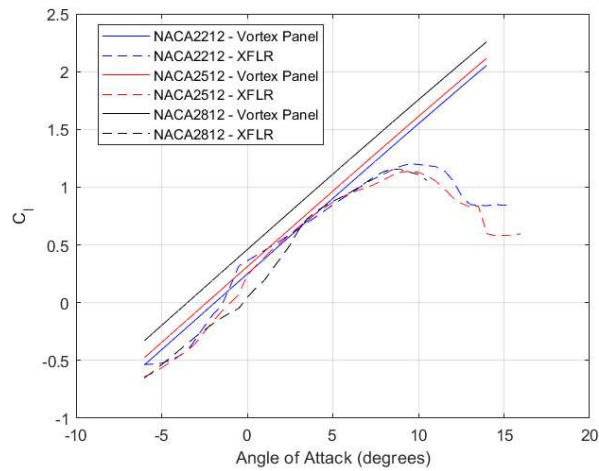


Figure 1.6.2. Comparison of airfoils with varying max camber location using Vortex Panel Method and XFLR5 at  $Ma = 0.4$

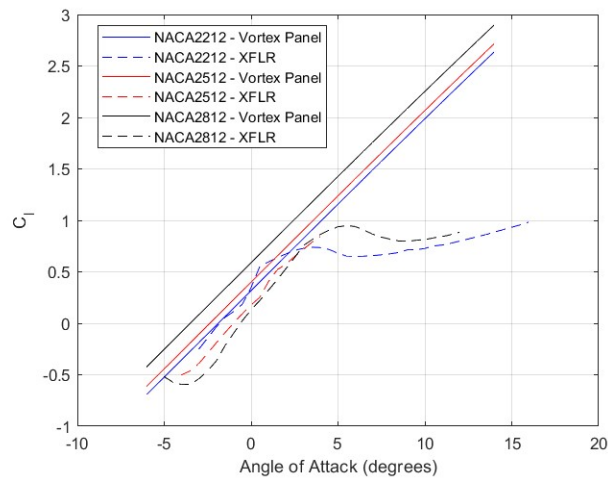


Figure 1.6.3. Comparison of airfoils with varying max camber location using Vortex Panel Method and XFLR5 at  $Ma = 0.7$

When comparing individual airfoils, consistently it can be observed that the forward camber locations are more consistent with the results from XFLR5. As the max camber is shifted towards the trailing edge this consistently is lost even at low angles of attack. Another observation discussed in the section on the effects of Mach number is that stalling begins at lower angles of attack with increasing Mach number, and this is consistent with each airfoil individually. To draw a comparison between airfoils, the location of max camber affects where stalling will occur. In Figure 1.6.1, at low Mach numbers, stalling occurs at lower angles of attack in aft camber positions. However, as the Mach number increases, this trend shifts to where aft camber positions are favored for resisting stall at high, sub-sonic Mach numbers as seen in Figure 1.6.3.

## 2. 3D Analysis

The remainder of the analysis will consider finite-length wings with zero twist, comprised of a thin, symmetric airfoil section throughout the span.

### 2.1. Lifting Line Theory

Prandtl's Lifting Line Theory is compressed of placing a bound vortex, or the lifting line, and an infinite number of horseshoe vortices that create a vortex sheet that is symmetric about the root of all the wings that will be observed in this analysis. These horseshoe vortices induce what is called downwash on the flow. This downwash results in an induced angle of attack which can be quantified by,

$$\alpha_i(y_0) = -\frac{w(y_0)}{V_\infty} \quad (5.17)$$

where,  $w$  is the downwash. Therefore, the angle of attack can be described by,

$$\alpha_{eff} = \alpha - \alpha_i \quad (5.1)$$

#### 2.1.1. Elliptic Solution

For a wing with an elliptical circulation distribution, the circulation distribution can be described by

$$\Gamma(y) = \Gamma_0 \sqrt{1 - \left(\frac{2y}{b}\right)^2} \quad (5.31)$$

where  $\Gamma_0$  is the circulation at the root. For elliptical wing in consideration the following is true,

$$C_L = 2\pi(\alpha_{eff}) \quad (5.19)$$

$$\Gamma_0 = \frac{2V_\infty SC_L}{b\pi} \quad (5.40)$$

$$\alpha_i = \frac{\Gamma_0}{2bV_\infty} \quad (5.36)$$

By use of equations 5.1, 5.19, 5.40, and 5.36, the following relationship can be found,

$$\frac{\Gamma_0}{2bV_\infty} = \frac{\alpha}{\frac{AR}{2} + 1}$$

and by multiplying each side by the radical of equation 5.31, the following equation is found to relate angle of attack to the circulation distribution,

$$\frac{\Gamma(y)}{2bV_\infty} = \frac{\alpha \sqrt{1 - \left(\frac{2y}{b}\right)^2}}{\frac{AR}{2} + 1}$$

Plotting this result across the span at various angles of attack can be seen in Figure 2.1.1.

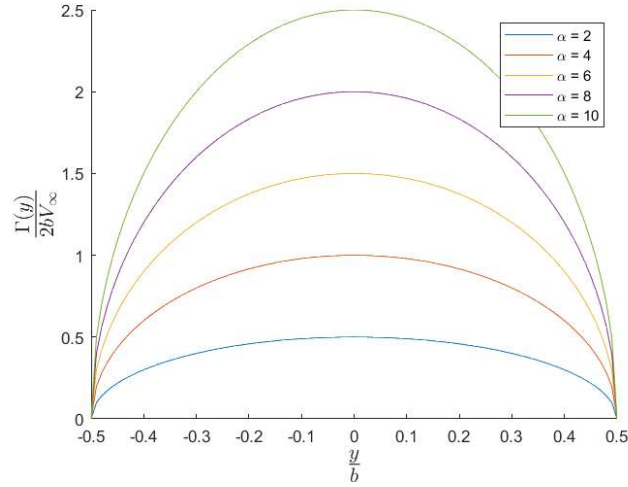


Figure 2.1.1. Correlation between circulation distribution and location across the span with angle of attack as a parameter.

By the results of  $\frac{\Gamma_0}{2bV_\infty}$ , the lift coefficient can be determined across a range of alpha through equation 5.42, below, and 5.36 from above.

$$\alpha_i = \frac{C_L}{\pi AR} \quad (5.42)$$

This results in a correlation between angle of attack and lift coefficient in Figure 2.1.2.

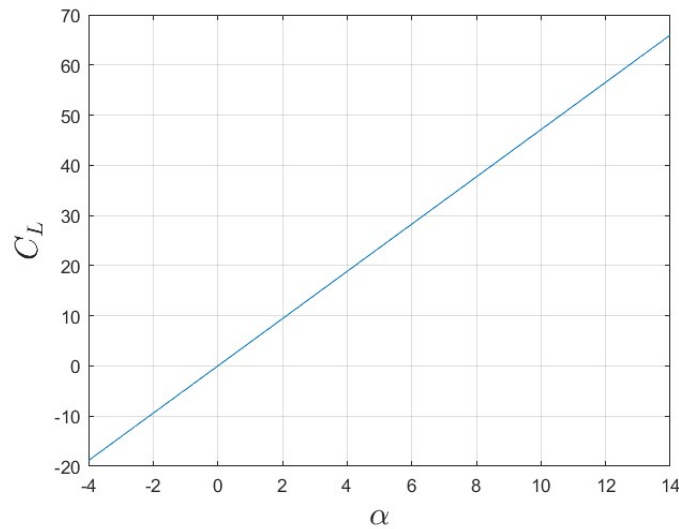


Figure 2.1.2. Lift coefficient vs angle of attack for an elliptic wing.

The results from Figure 2.1.2 can be used to determine a distribution of induced drag by use of,

$$C_{Di} = \frac{C_L^2}{\pi AR} \quad (5.43)$$

The results from equation 5.43 with varying angle of attack produce the correlation in Figure 2.1.3.

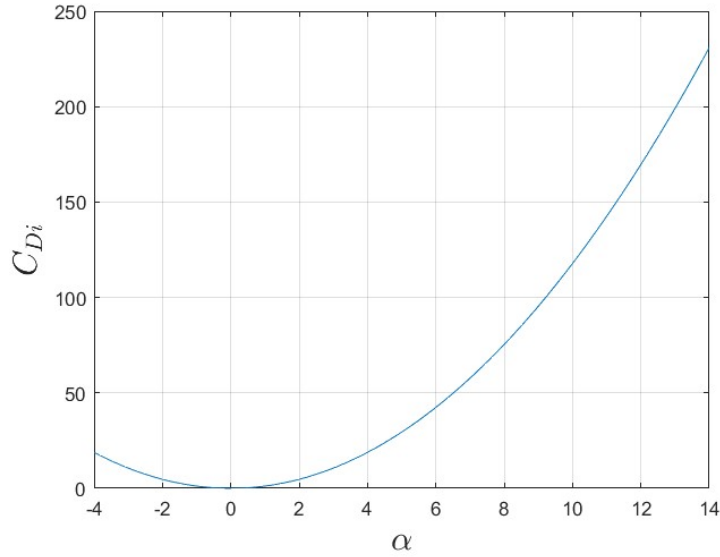


Figure 2.1.3. Induced drag coefficient vs angle of attack for an elliptic wing.

## 2.1.2. General Solution

For the general solution to Lifting Line Theory, coefficients for the following Fourier Series are governed by,

$$\alpha(\theta_0) = \frac{2b}{\pi c(\theta_0)} \sum_1^N A_n \sin n\theta_0 + \alpha_{L=0}(\theta_0) + \sum_1^N \frac{nA_n \sin n\theta_0}{\sin \theta_0} \quad (5.51)$$

Where  $N$  is the number of terms and  $\theta_0$  is a location on the wing. Therefore, to determine  $N$  coefficients,  $N$  locations on the wing need to be evaluated. Table 1 shows the locations that were used to determine 16 coefficients,  $A_n/\alpha$ , and Table 2 shows the values of  $A_n/\alpha$  that the system of equations converged on.

Table 1. Theta values to evaluate general solution coefficients.

Equation #	$\theta_0$
1	0.001
2	0.2103
3	0.4196
4	0.6289
5	0.8382
6	1.0475
7	1.2567
8	1.4661
9	1.6754
10	1.8848
11	2.0941
12	2.3034
13	2.5127
14	2.7220
15	2.9313
16	3.1406

Table 2. Results of Fourier Coefficients

n	$A_n/\alpha$
1	0.2403
2	0
3	0.0292
4	0
5	0.0062
6	0
7	0.0018
8	0
9	0.0006
10	0
11	0.0002
12	0
13	0
14	0
15	0.0007
16	0

As the number of terms used in the series increased the terms converged to similar values as seen in Figure 2.1.4. After approximately 5 or 6 terms, the convergence is minimal.

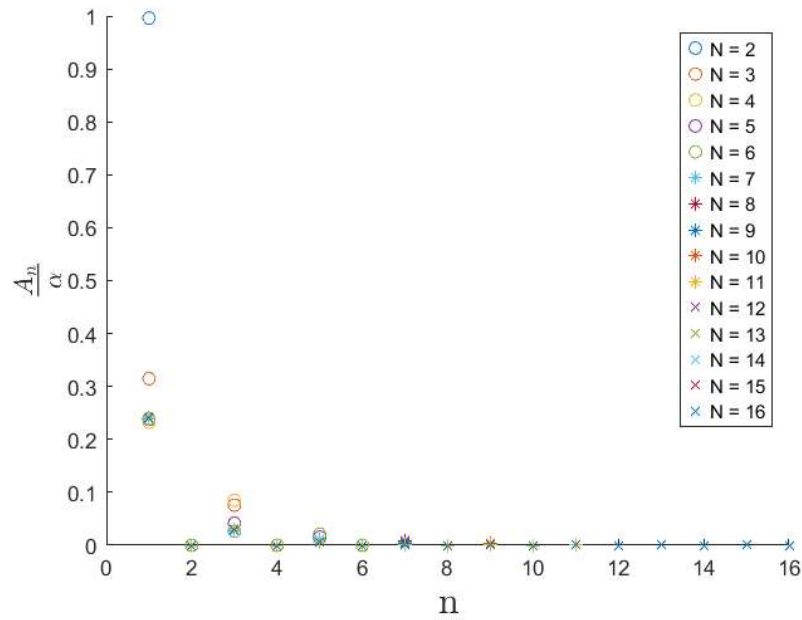


Figure 2.1.4. Fourier Coefficient Values with increasing number of terms evaluated.

Using the 16-coefficient, a relationship between  $\frac{\Gamma(y)}{2bV_\infty}$  and  $\frac{y}{b}$  can be found by these two equations,

$$\Gamma(\theta) = 2bV_\infty \sum_{n=1}^N A_n \sin n\theta \quad (5.48)$$

$$y = -\frac{b}{2} \cos \theta \quad (5.46)$$

The results of evaluating these equations from one tip of the wing to the other can be seen in

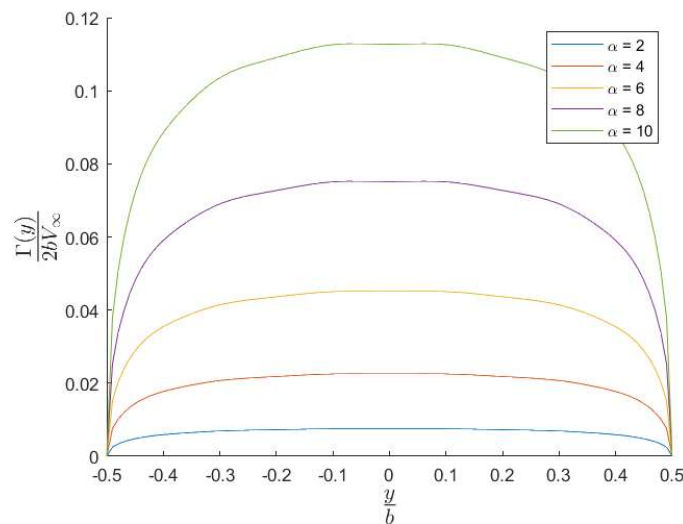


Figure 2.1.5. General Solution across a wing with the angle of attack as a parameter.

These results show that with increasing the angle of attack, circulation increases, and the circulation goes to zero at the tips. Both of which are expected results. Using equations 5.48 and 5.46, a relationship between  $\frac{\Gamma(y)}{2bV_\infty\alpha}$  and  $\frac{y}{b}$  can be found with the number of terms,  $N$ , as a parameter. This relationship is shown in Figure 2.1.6.

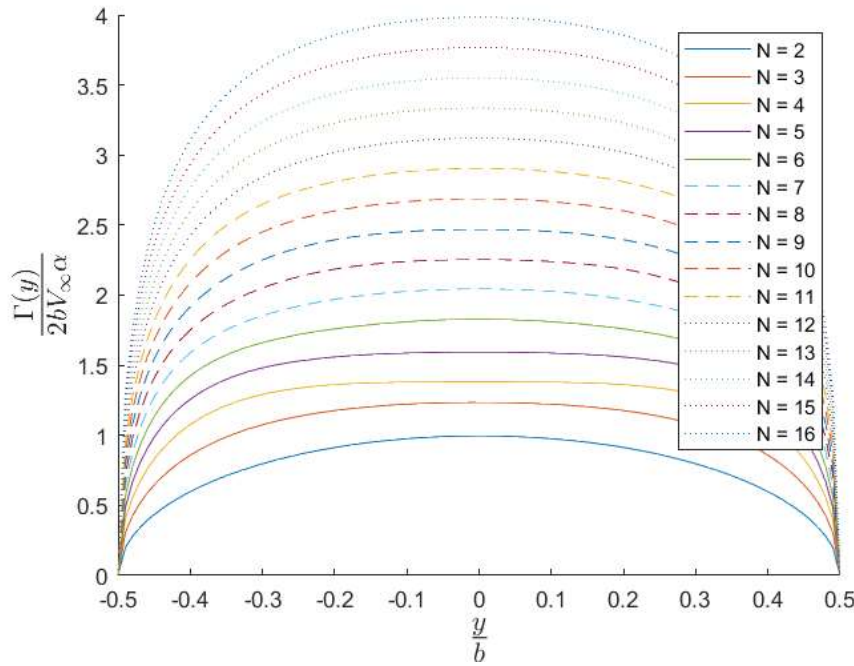


Figure 2.1.6. General Solution across a wing with  $N$  as a parameter.

Going back to the 16-term series lift and induced drag coefficients can be calculated by use of,

$$C_L = A_1 \pi AR \quad (5.53)$$

and,

$$C_{D,i} = \frac{C_L^2}{\pi AR} (1 + \delta) \quad (5.61)$$

where,

$$\delta = \sum_{n=2}^N n \left( \frac{A_n}{A_1} \right)^2$$

Since, the coefficients to the Fourier Series were found in terms of  $A_n/\alpha$  both may be written as functions of angle of attack. The plots of each function are shown in

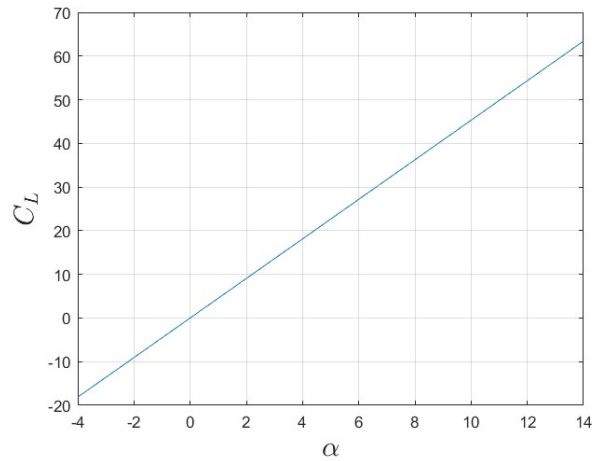


Figure 2.1.7. Lift coefficient vs angle of attack for a straight wing.

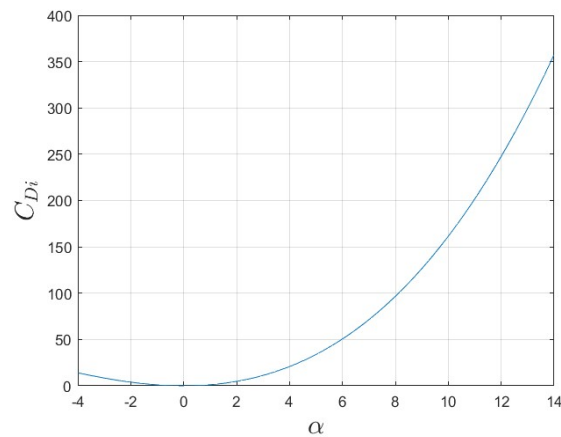


Figure 2.1.8. Induced drag coefficient vs angle of attack for a straight wing.

### 2.1.3. Discussion

Figure 2.1.2 and Figure 2.1.7, as well as, Figure 2.1.3 and Figure 2.1.8 are inspected to create a comparison for the lift coefficient and induced drag coefficient, respectively, between the elliptic wing and straight wing. The two wings are very similar in lift coefficients across a range of low angles of attack. As for the induced drag coefficients, the two are very comparable in shape and in magnitude in angles of attack under  $6^\circ$ , however, based on these models, the straight wing will experience an increase in induced drag above  $6^\circ$  compared to that of the elliptic wing. This increase in induced drag is due to an increased tip vorticity and thus downwash in the straight wing.



## 2.2. Taper Ratio

The taper ratio can be defined as,

$$q = 1 - \frac{c_t}{c_r}$$

where  $c_t$  is the cord length at the tip and  $c_r$  is the cord length at the root. The aspect ratio must remain constant between wings, therefore, the cord lengths at the root and tip for each wing are defined by,

$$c_r = \frac{1}{AR(2 - q)}$$

$$c_t = (1 - q)c_r$$

Table 3 shows the five wing parameters that will be analyzed in this section. All wings will have a span of 1 and airfoil shape of NACA 0012 throughout the span. Aspect ratio is set to 6.

*Table 3. Wing parameters for taper ratio analysis.*

Taper Ratio	$c_r$ (m)	$c_t$ (m)
0.00	0.1667	0.1667
0.23	0.1883	0.1450
0.46	0.2165	0.1169
0.69	0.2545	0.0789
0.91	0.3030	0.0303

The preceding parameters were evaluated in XFLR5 at 50 m/s and an angle of attack of  $1^\circ$ . To determine the correction factors,  $\delta$  and  $\tau$ , the following equations were used.

$$C_{D,i} = \frac{C_L^2}{\pi AR} (1 + \delta) \quad (5.61)$$

$$a = \frac{a_0}{1 + \left(\frac{a_0}{\pi AR}\right) (1 + \tau)} \quad (5.70)$$

In equation 5.70,  $a$  was determined by utilizing adjacent points to  $1^\circ$  to determine a  $\frac{dc_l}{d\alpha}$ . Evaluating equations 5.61 and 5.70 for  $\delta$  and  $\tau$ , respectively, at for each set of parameters, yields the correlation in

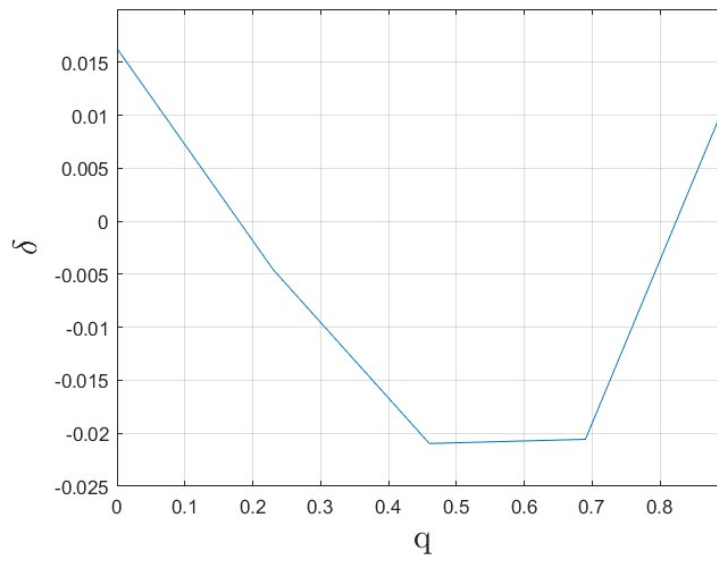


Figure 2.2.1. Delta vs taper ratio with constant aspect ratio

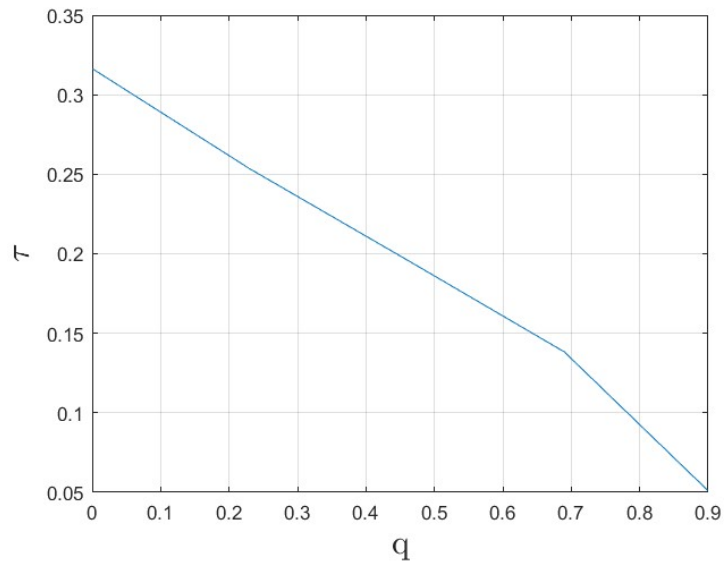


Figure 2.2.2. Tau vs taper ratio with constant aspect ratio

From the given set of 5 wings with varying taper ratios,  $\delta$  follows a parabolic distribution with increasing taper ratios while being minimized when the taper ratio is in the 0.4 to 0.7 range. However, the taper ratio has a near linear effect on  $\tau$  in the range of taper ratios from 0 to 0.9. As stated in Anderson, values of  $\tau$  fall in the range of 0.25 to 0.05, which is accurately observed in Figure 2.2.2.

## 2.3. Aspect Ratio

This section will discuss the effects of varying the Aspect Ratio of a wing which is defined by,

$$AR = \frac{b^2}{S}$$

Where  $b$  is the span and  $S$  is the planform area of the wing. Given the aspect ratio,  $\frac{dc_l}{d\alpha}$  can be determined from the previously discussed equation 5.70 and approximating  $\tau$  at a constant value of 0.316 as determined for a taper ratio of 0 in the previous section. Combining this result with equation 5.19,  $c_l$  can be determined as a function of angle of attack for a symmetric airfoil ( $\alpha_{L=0} = 0^\circ$ ). Plotting this result across various aspect ratios can be seen in Figure 2.3.1.

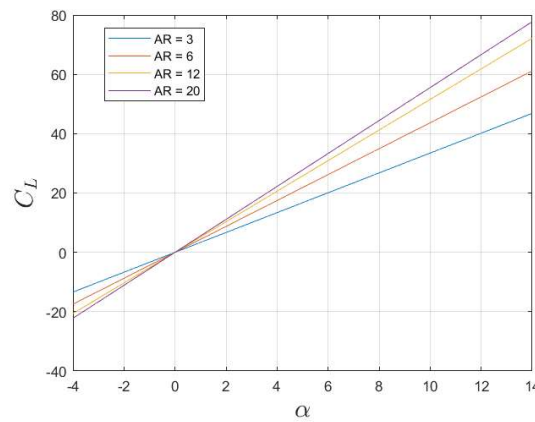


Figure 2.3.1. Lift coefficient vs angle of attack for varying aspect ratios.

From the results of the equation 5.70 and Figure 2.3.1 the aspect ratio has a direct effect on the slope of  $c_l$  vs  $\alpha$ . The observation that increasing aspect ratios leads to increasing slopes also aligns with intuition that more area on a wing would lead to an increase in lift.

## 3. Conclusion

The aerodynamic characteristics of airfoils and finite wings were analyzed by examining key geometric traits, including airfoil shape, angle of attack, taper ratio, and aspect ratio. Additionally, the performance of a wing is influenced by flow parameters such as Reynolds number and Mach number, which play a critical role in determining aerodynamic behavior. With various models and correction factors, the effects of these parameters can be predicted, however each method has its own limitations.

For two-dimensional airfoils, Thin Airfoil Theory, the Vortex Panel Method, and XFLR5 were employed to evaluate aerodynamic performance. In the case of finite wings, Lifting Line Theory and XFLR5 were utilized to assess the influence of specific parameters on lift and overall performance. These methodologies provide valuable insights into the complex interactions between geometry, flow conditions, and aerodynamic efficiency, contributing to a better understanding of wing and airfoil behavior.